ACS APPLIED ENERGY MATERIALS

www.acsaem.org Article

Disentangling Energy Transfer Pathways in Donor–Acceptor Dyads: A Molecular-Level Perspective for TADF OLED Applications

Published as part of ACS Applied Energy Materials special issue "Computational Energy Materials Discovery".

Nikhitha R and Anirban Mondal*

Cite This: https://doi.org/10.1021/acsaem.5c01620 Read Online

ACCESS | Metrics & More | Article Recommendations | Supporting Information

ABSTRACT: A comprehensive understanding of the nonradiative energy transfer process is critical for advancing emitter design in organic light-emitting diodes (OLEDs). This study employs a multiscale computational approach integrating classical molecular dynamics, quantum chemical calculations, and kinetic Monte Carlo simulations to investigate a multiresonant (MR) emitter dyad (Cy-tmCPBN) in pure and doped film morphologies. Our results show that film morphology and molecular orientation critically influence energy transfer efficiency. In the pure film, tight molecular packing and favorable donor–acceptor alignment promote efficient intermolecular energy transfer. In contrast, doping with a donor host (Cy-tmCP)—which incorporates the same donor fragment as Cy-tmCPBN—introduces spatial dilution and disrupts molecular alignment, yielding reduced resonance energy transfer rates. Quantum mechanical analyses based on interfragment charge transfer and noncovalent interaction frameworks reveal that while the excitations are predominantly localized, weak yet non-negligible intermolecular electronic coupling in the pure film facilitates the observed energy transfer. These findings underscore the importance of tuning molecular organization and structural rigidity to control exciton behavior and optimize energy transfer in OLED emitter layers, aligning with ongoing efforts to improve device performance through rational molecular design.

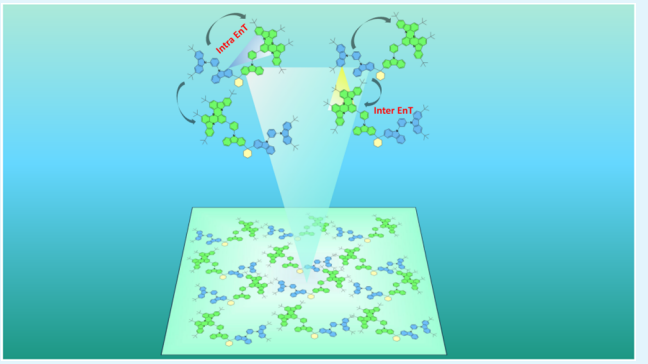

KEYWORDS: *thermally activated delayed fluorescence (TADF), resonance energy transfer (RET), organic light-emitting diodes (OLEDs), multiscale simulations, exciton dynamics*

1. INTRODUCTION

In 2000, Forrest et al. reported the first highly efficient fluorescent organic light-emitting diode (OLED) by employing a phosphorescent sensitizer to harvest triplet excitons via nonradiative energy transfer mechanisms.[1] These sensitized OLEDs' internal quantum efficiency (IQE) approached 100%, owing to efficient long-range energy transfer from the triplet donor to a fluorescent emitter. These systems demonstrated high electroluminescence (EL) efficiency and excellent color purity.[2,3] However, the dependence on heavy-metal-based phosphorescent sensitizers remains a significant drawback due to their high cost and limited sustainability.[4] In response, the field saw a transformative advancement in 2012, when Adachi and co-workers introduced a new class of purely organic emitters exhibiting thermally activated delayed fluorescence (TADF).[5] These materials were molecularly engineered to enable efficient reverse intersystem crossing (RISC) by minimizing the singlet–triplet energy gap, thus allowing nonradiative triplet excitons to be upconverted into radiative singlet states. TADF compounds quickly emerged as promising alternatives to metal-based sensitizers, reinvigorating interest in designing purely organic systems for high-efficiency OLEDs.[4]

In contemporary OLED architectures, intermolecular energy transfer—particularly Förster resonance energy transfer (FRET)—plays a pivotal role in enhancing emission efficiency by facilitating the transfer of excitation energy from host materials to guest emitters.[6−8] Integrating TADF sensitizers with conventional fluorescent emitters has been especially impactful, improving device stability and color purity.[8,9] In so-called hyperfluorescent systems, efficient FRET from the singlet excited state of the TADF molecule to the singlet state of the fluorescent emitter enables prompt fluorescence with reduced reliance on repeated RISC processes.[6] However, competing energy transfer pathways at the nanoscale can detrimentally

Received: May 29, 2025
Revised: July 9, 2025
Accepted: July 10, 2025

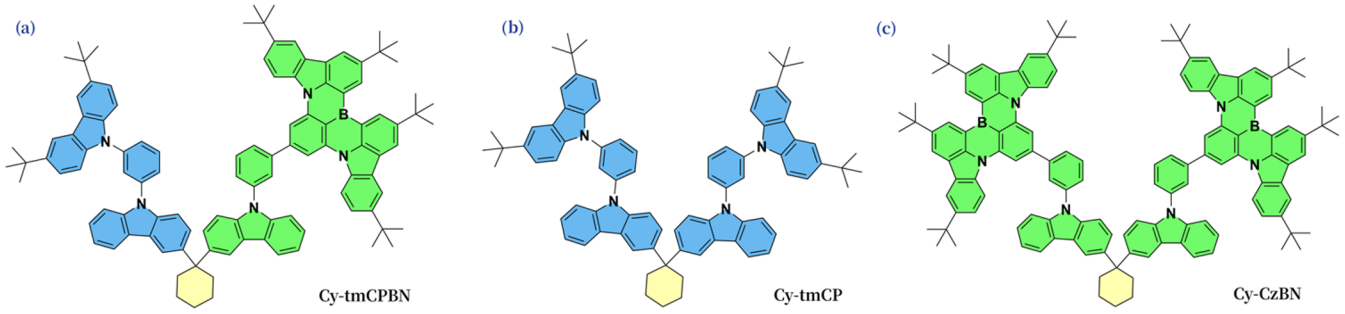

Figure 1. Representative molecular structures: (a) the dyad molecule employed in the active layer of the OLED, (b) the donor dyad serving as the host in the doped system, and (c) the emitter dyad where two CzBN units are linked via cyclohexane.

affect performance. One such pathway involves Dexter energy transfer, wherein excitation energy is transferred from the triplet state of the TADF sensitizer to the triplet state of the emitter through short-range orbital overlap. This process, which leads to the formation of nonemissive triplet states on the emitter, can significantly quench emission and reduce overall device efficiency.[6,10] In addition to energy transfer mechanisms, charge transfer interactions—either through-bond (TBCT) or through-space (TSCT)—also play a critical role in determining excited-state dynamics.[11−13] Particularly in TSCT-based systems, noncovalent spatial arrangements between donor and acceptor units facilitate effective orbital separation, resulting in a small singlet−triplet energy gap (ΔE_{ST}) and high photoluminescence quantum yield (PLQY).[14,15] These diverse pathways underscore the complexity of exciton dynamics and energy transport in OLED systems, highlighting the need to dissect individual contributions to guide rational molecular design.

Resonance energy transfer (RET) is a nonradiative process in which electronic excitation energy is transferred from an excited donor molecule to a neighboring acceptor located within a sub-10 nm distance. Termed "resonant" due to the simultaneous de-excitation of the donor and excitation of the acceptor without photon emission, this process involves no net energy loss. The theoretical foundation of RET was established by Förster, who applied perturbation theory to describe its distance-dependent efficiency.[16] In contrast to Dexter energy transfer, which requires significant orbital overlap, RET operates effectively over longer distances—typically in the 1−10 nm range—where such overlap is negligible. However, the donor and acceptor must remain sufficiently close that the transfer is still nonradiative, occurring over a distance shorter than the wavelength corresponding to donor emission or acceptor absorption.

Molecular dyads—covalently linked donor−acceptor systems—have been extensively studied in the context of biological sensing, fluorescent labeling, and photoinduced electron or energy transfer in both organic molecules and metal complexes.[17−19] More recently, these constructs have been found to be relevant in optoelectronic applications.[20] Notably, Kwon et al. reported a functional dyad (Cy-tmCPBN) designed for OLED applications, in which a donor unit structurally analogous to the host molecule (Cy-tmCP) was linked to a multiresonant TADF (MR-TADF) acceptor (Cy-CzBN) via a nonconjugated cyclohexane bridge.[20] This molecular architecture facilitated efficient intramolecular energy transfer in solution while incorporating a cyclohexane linker improved solubility and film-forming properties by introducing nonplanarity that helps suppress aggregation driven by strong $\pi-\pi$ interactions. While their study primarily focused on energy transfer in dilute toluene solution, the behavior of the dyad in the condensed phase—particularly in neat films relevant to device applications—remains largely unexplored. Given the nanostructured nature of OLED active layers, where donor−acceptor molecules self-assemble into amorphous or weakly ordered domains, understanding how nanoscale morphology and intermolecular coupling modulate energy transfer is essential. In particular, the extent to which intermolecular interactions contribute to energy transfer efficiency in the solid state has yet to be systematically investigated.

In this work, we present a comprehensive computational investigation into the energy transfer mechanisms within molecular dyads designed for OLED applications, with a particular emphasis on disentangling the roles of intra- and intermolecular interactions. By combining molecular dynamics (MD) simulations with quantum mechanical (QM) calculations, we explore a multiscale approach that, to our knowledge, has not been previously applied in detail to such dyad systems. Our results reveal that intermolecular interactions within the amorphous solid film play a pivotal role in governing the overall energy transfer dynamics, often rivaling or even surpassing the contributions from intramolecular pathways. These findings challenge the prevailing assumption that energy transfer in such dyads is primarily intramolecular, as inferred from solution-phase studies,[20] and instead highlight the importance of collective effects in the condensed phase. This subtle understanding highlights the need to account for molecular packing, dynamic conformations, and spatial arrangements in real device-relevant environments. Elucidating the delicate interplay between intra- and intermolecular energy transfer processes, our study provides valuable design principles for enhancing energy transfer and emission efficiency in dyadic systems. In particular, by highlighting the nanoscale interplay between molecular design and supramolecular assembly, we offer critical insights for the rational design of next-generation OLED materials and organic nanophotonic systems. Ultimately, these findings pave the way for engineering high-performance OLED materials with improved efficiency, stability, and color purity.

2. METHODS

The representative molecular structures used in this study are shown in Figure 1. For clarity and consistency with the nonradiative energy transfer process, we refer to the MR core as the acceptor throughout this work. To investigate resonance energy transfer in molecular dyads, we employed a multiscale computational framework inspired by the methodology of Anzola et al.,[16] which integrates molecular dynamics simulations, quantum mechanical calculations, and a coarse-grained kinetic model. This approach comprehensively explores structural dynamics and electronic interactions across different length and time

https://doi.org/10.1021/acsaem.5c01620
ACS Appl. Energy Mater. XXXX, XXX, XXX−XXX

scales. The nonbonded parameters for MD simulations were derived using the SOBTOP package,[21] which also provided atom types and bonded parameters. Partial atomic charges were obtained through a restrained electrostatic potential (RESP) fitting procedure using the Multiwfn package,[22] ensuring an accurate representation of electrostatic interactions. All MD simulations were carried out using GROMACS 2020.4 package[23,24] to sample conformational dynamics in both solution and solid-state environments reliably.

To model the solid-state morphology of the dyad systems, we carried out ground-state MD simulations that mimicked the practical conditions of film formation via a thermal annealing protocol in the NPT ensemble. A total of 500 dyad molecules were packed into a cubic box with a side length of 10 nm. Initially, the system was energy-minimized using the steepest-descent algorithm to eliminate unfavorable contacts and relax the molecular packing. This was followed by a gradual heating phase, where the system was annealed from 100 to 800 K over 3 ns using a canonical velocity-rescaling thermostat[25] and a Berendsen barostat[26] to maintain pressure. Long-range electrostatic interactions were treated using the smooth particle mesh Ewald (PME) method,[27] while a real-space cutoff of 1.3 nm was applied for nonbonded interactions. After annealing, the system was cooled stepwise to stabilize the amorphous morphology from 800 to 600 K and then from 600 to 300 K, with each stage lasting 3 ns under NPT conditions. This controlled cooling allowed the molecules to self-assemble into a realistic, kinetically trapped configuration representative of experimentally relevant film structures.[28] Following thermal equilibration, 3 ns production simulations were performed in the NVT ensemble at 300 K to capture the dynamic behavior under equilibrium conditions. The velocity Verlet algorithm was used for time integration with a 1 fs time step. To investigate the influence of doping, a doped film was constructed by embedding the dyad species at a 12 mol % concentration into a host dyad matrix. To achieve the 12 mol % concentration, 60 dyad molecules were packed in a cubic box with a side length of 10 nm along with 440 host molecules. The same annealing and equilibration protocol was applied to this system. Comparative analysis of the neat and doped films enabled us to probe differences in ground-state morphology and intermolecular interactions, providing insights into the structural basis of energy transfer efficiency in these systems.

The excited-state properties of the donor and multiresonant fragments were computed using time-dependent density functional theory (TD-DFT) at the B3LYP/6−31G(d,p) level. Both ground-state and first excited-state geometries were fully optimized prior to evaluating excitation energies and transition dipole moments, as implemented in the Gaussian 09 software package.[29] To evaluate the time-dependent electronic coupling following excitation, we employed a non-equilibrium molecular dynamics (NEMD) protocol in which the donor moiety (D) was electronically excited (D*) at $t = 0$, while retaining its ground-state geometry. This sudden excitation mimics the vertical Franck−Condon transition and allows monitoring of coupling fluctuations over time. Although this approach neglects structural relaxation in the excited state, the rigid nature and low reorganization energy of the MR-TADF dyad minimize the associated error, making the method suitable for capturing exciton dynamics in these systems. MD trajectories were sampled every 40 ps, from which 16 snapshots were randomly selected to ensure representative and unbiased coverage of the conformational space. All simulations employed a 1 fs time step. To capture statistically meaningful excited-state dynamics, the snapshots were extracted from the initial 3 ns of the ground-state MD trajectory. These snapshots served as starting points for a series of non-equilibrium molecular dynamics simulations of the D*A system, where energy transfer proceeds from the excited donor to the ground-state acceptor.[16] Each NEMD simulation was run for 15 ns to generate sufficiently long trajectories for detailed analysis. The figures shown correspond to a representative trajectory sampled from the NEMD simulations. In these NE trajectories, the geometry of the excited donor was kept fixed to that of the ground-state configuration, thus approximating vertical excitation and focusing purely on the energy transfer dynamics without including geometry relaxation effects.

Resonance energy transfer is a nonradiative process through which an electronically excited donor (D*) transfers its excitation energy to a nearby acceptor (A), resulting in the donor returning to its ground state and the acceptor being excited.

$$D^*A \rightarrow DA^* \tag{1}$$

When the intermolecular interaction between the donor and acceptor can be approximated by point dipoles, the squared coupling strength can be estimated using[16]

$$|V_{DA}|^2 = \frac{K^2 |\mu_D|^2 |\mu_A|^2}{(4\pi\epsilon_0)^2 \eta^4 r^6} \tag{2}$$

where μ_A and μ_D correspond to the transition dipole moments associated with D fluorescence and A absorbance, r is the intermolecular distance, η is the refractive index, and K^2 is the orientation factor between the two dipoles and ranges from 0 to 4.[30] The dynamic orientation factor, K^2, was calculated using the following expression:[31]

$$K^2 = (\cos\theta_{DA} - 3\cos\theta_D \cos\theta_A)^2 \tag{3}$$

where θ_{DA} is the angle between the donor and acceptor transition dipole moments (μ_D and μ_A), while θ_D and θ_A denote the angles between the donor and acceptor transition dipoles and the unit vector e, which points from the donor to the acceptor, respectively.

The RET rate can be estimated as

$$k_{RET} = (\hbar^2 c)^{-1} |V_{DA}|^2 J \tag{4}$$

where $J = \int_0^\infty F_D(\tilde{\nu}) A_A(\tilde{\nu})\, d\tilde{\nu}$ denotes the spectral overlap integral between the normalized donor emission spectrum (F_D) and acceptor absorption spectrum (A_A), expressed in centimeters (cm). Here, c is the speed of light in cm/s. To account for the orientational arrangement of molecules in the solid-state film, we calculated the order parameter S using

$$S = \frac{3\langle\cos^2\theta\rangle - 1}{2} \tag{5}$$

where θ is the angle between the transition dipole moment and the reference axis (typically the surface normal). In our system, we defined θ as the angle between the transition dipole moment of each individual donor and acceptor fragment obtained from QM calculations and the surface normal. An S value of 1 corresponds to perfect vertical alignment, 0 indicates isotropic orientation, and −0.5 represents perfect horizontal alignment.[32] This orientational analysis provides insight into how molecular packing influences energy transfer efficiency in the thin film environment.

For each non-equilibrium trajectory, we evaluated the time-dependent donor−acceptor coupling V_{DA} using eq 2. The refractive index η was fixed at 1.45, consistent with prior studies on organic molecules.[16] This value represents a typical optical dielectric constant for amorphous organic materials in the visible range and provides a reasonable approximation for evaluating Förster transfer rates in disordered morphologies.[33] The transition dipole moments μ_D and μ_A were extracted from TD-DFT calculations at the B3LYP/6−31G(d,p) level and were treated as constant in magnitude throughout the simulation. Variations in the donor−acceptor coupling over time arose solely from changes in the relative orientations of the dipoles, as captured by the orientation factor K^2. Subsequently, the time-resolved resonance energy transfer rate k_{RET} was computed using eq 4, incorporating a spectral overlap integral $J = 5.8 \times 10^{-9}$ cm, obtained from the computed overlap between the donor's emission spectrum and the acceptor's absorption spectrum. The spectrum was simulated using Franck−Condon vibronic analysis, based on ground- and excited-state frequency calculations, with toluene as the solvent to reflect experimental conditions. All trajectory analyses, including the extraction of dipole orientations and calculation of k_{RET}, were conducted using the MDAnalysis Python package.[34,35]

To investigate the decay kinetics of the dyad system, we employed a coarse-grained kinetic Monte Carlo (kMC) simulation framework that leveraged the time-resolved resonance energy transfer rates, k_{RET}, obtained from non-equilibrium trajectories. For each of the N sampled

https://doi.org/10.1021/acsaem.5c01620
ACS Appl. Energy Mater. XXXX, XXX, XXX−XXX

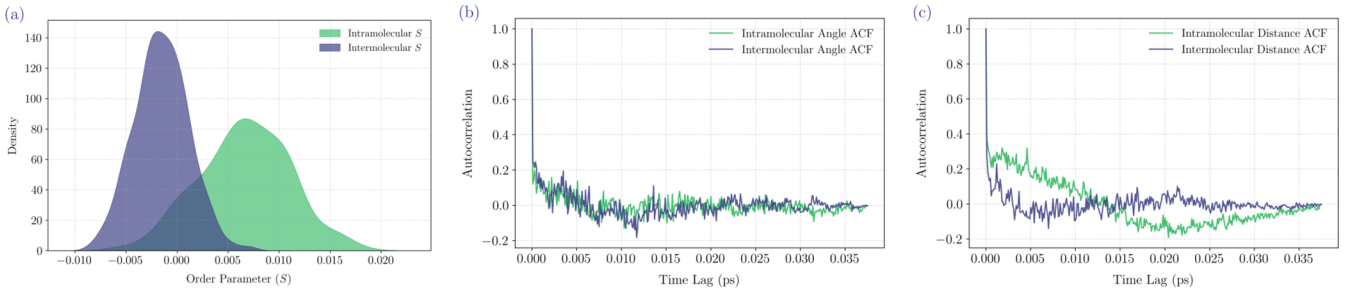

Figure 2. (a) Distribution of the order parameter S for the pure dyad film, indicating overall isotropic molecular orientation with subtle intra- and intermolecular alignment preferences. (b) Angular autocorrelation functions show rapid decay of orientational correlations, reflecting dynamic molecular reorientation. (c) Distance autocorrelation functions highlight distinct temporal behaviors, with constrained intramolecular oscillations and faster decorrelation in intermolecular distances.

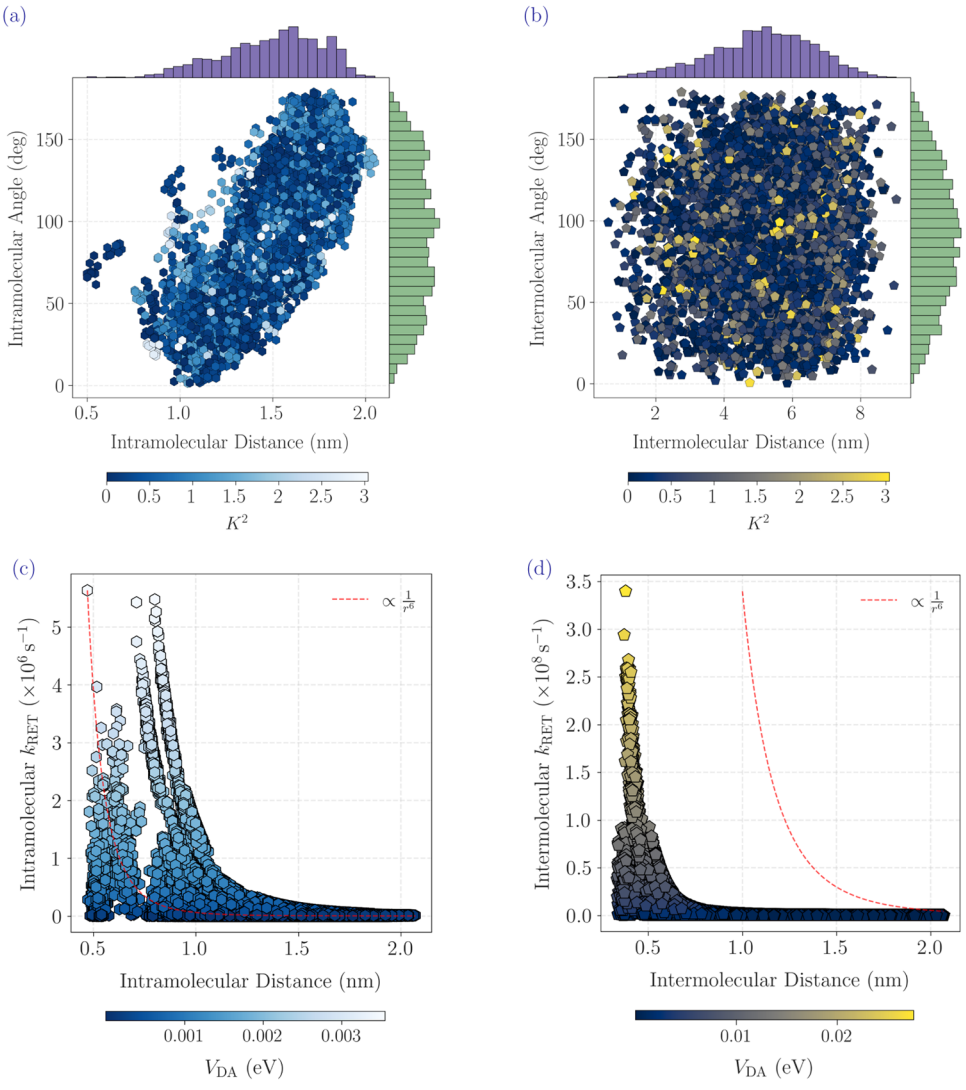

Figure 3. (a) Joint distribution of distance, angle, and orientation factor (K^2) for intramolecular donor−acceptor (D-A) pairs in the pure dyad film, highlighting linker-constrained conformations. (b) Corresponding distribution for intermolecular D−A pairs, showing more random geometries but occasional high K^2 values. (c) RET rates (k_{RET}) versus electronic coupling (V_{DA}) for intramolecular interactions illustrate a distance-dependent trend. (d) k_{RET} versus V_{DA} for intermolecular interactions, showing significantly higher rates enabled by stronger couplings despite larger separations. The dashed red line in panels (c) and (d) represents a fit to the $\frac{1}{r^6}$ dependence, indicating that the k_{RET} rates follow this characteristic distance dependence.

NE trajectories, we evaluated k_{RET} at every time step to compute the instantaneous probability of energy transfer from the excited donor (D*) to the acceptor (A). This probability was then compared against a randomly generated number to determine whether the system would undergo an energy transfer event or remain in its current state. The simulation proceeded until energy transfer occurred, at which point the corresponding decay time was recorded. A similar procedure was applied to the doped system to assess how the presence of the host matrix modulated the excited donor (D*) decay behavior. Specifically, while the energy transfer rates were calculated with nanosecond time

https://doi.org/10.1021/acsaem.5c01620
ACS Appl. Energy Mater. XXXX, XXX, XXX−XXX

resolution to capture the rapid electronic transitions, the overall decay of the excited-state donor population (D*), as obtained from the ensemble of stochastic trajectories, was analyzed on the microsecond time scale. This coarse-grained, long-time scale behavior is in excellent agreement with the experimentally observed delayed fluorescence lifetime of the Cy-tmCPBN dyad.[20]

To complement these dynamic simulations, we further analyzed the excitonic characteristics of both the neat and doped dyad films using quantum mechanical methods. To analyze the electronic interactions between donor and acceptor fragments, we constructed representative dimer structures and optimized the ground states using the semi-empirical extended tight-binding (xTB) method[36] to obtain their lowest energy configurations. This approach avoids bias toward extreme spatial arrangements (e.g., closest or most distant neighbors) and allows for a physically meaningful assessment of intermolecular interactions based on thermodynamically stable geometries. Excited-state calculations were carried out within the Tamm-Dancoff approximation (TDA-DFT) using both B3LYP/6−31G(d,p) and PBE0/6−31G(d,p) methods as implemented in the ORCA program,[37] with the latter selected based on its reported accuracy for TADF-dimer systems.[38] The consistency between results obtained from both methods confirms the robustness of our electronic structure analysis. We computed density difference plots, transition density matrices, and interfragment charge transfer (IFCT) values using the Multiwfn package to gain deeper insight into exciton localization and charge redistribution. In addition, the nature and strength of noncovalent interactions within the dimers were analyzed using the Independent Gradient Model based on Hirshfeld partitioning (IGMH),[39] providing a detailed view of the supramolecular interactions governing energy transfer efficiency.

3. RESULTS AND DISCUSSION

We begin our analysis with the pure dyad system to understand how molecular orientation and dynamic fluctuations within the thin film influence resonance energy transfer. The morphological characteristics of the film were first assessed using the orientational disorder parameter, S, as shown in Figure 2a. The distribution of S reveals that, on average, the film exhibits near-isotropic molecular orientation. However, individual molecules demonstrate slight preferences toward either horizontal or vertical alignment. Specifically, the intramolecular order parameter (green curve) is centered around a small positive value (∼0.01), suggesting a weak preference for horizontal alignment between adjacent dyads. Importantly, neither distribution approaches the theoretical limits of $S = 1$ (perfect vertical alignment) or $S = -0.5$ (perfect horizontal alignment), reaffirming that the system as a whole remains predominantly isotropic with only subtle directional biases. These orientation distributions have direct implications for RET, particularly in the context of the orientation factor K^2, which depends on the relative alignment of donor and acceptor dipoles. In our simulations, K^2 exhibits substantial fluctuations, ranging between 0 and 3 for both intramolecular and intermolecular donor−acceptor pairs (detailed discussion on Figure 3). This variability highlights that the commonly assumed isotropic average of $K^2 = 2/3$ may not be representative in systems with localized orientational heterogeneity, underscoring the importance of accounting for actual molecular arrangements in RET modeling.

To further probe the dynamics of molecular orientation, we examined the angular autocorrelation functions depicted in Figure 2b. Both intra- and intermolecular angle correlations decay rapidly—within ∼ 0.005 ps—indicating fast reorientation motion of molecular fragments. This rapid loss of orientational memory suggests that the values of S represent statistical averages over highly dynamic configurations rather than static alignments. Spatial dynamics were further characterized through distance autocorrelation functions (Figure 2c). Here, we observed a clear distinction between intra- and intermolecular components. The intramolecular distance ACF (green) retained a positive correlation for up to ∼ 0.01 ps, followed by oscillatory behavior indicative of periodic motion constrained by the cyclohexane linker. In contrast, the intermolecular ACF (blue) decayed more swiftly, suggesting greater spatial fluctuations between distinct dyad molecules. These differences in temporal correlation behavior reflect distinct kinetic regimes for energy migration, with intramolecular RET likely occurring in a more structurally constrained environment, while intermolecular RET proceeds under higher configurational variability.

To further elucidate the structural factors influencing resonance energy transfer in the pure dyad film, we analyzed both intramolecular and intermolecular donor−acceptor (D-A) configurations in terms of their geometries and associated electronic coupling strengths. D−A distances and angle distributions reveal marked differences between intramolecular and intermolecular pairs. Intermolecular distances span a broader range, from approximately 0.3 to 9 nm, while intramolecular distances are more tightly constrained between 0.4 and 2 nm (Figure 3). Similarly, both types of D−A angles exhibit broad variability, ranging from 0 to 175 degrees, yet the underlying patterns differ significantly. As shown in Figure 3a, intramolecular pairs exhibit a clear correlation between distance and angle, where an increase in the donor−acceptor core separation is accompanied by a rise in the corresponding angle. This structured trend reflects the conformational constraints imposed by the cyclohexane linker connecting the donor and acceptor units. The orientation factor K^2, depicted as a color scale, exhibits localized high values (up to 3) at specific geometric configurations, suggesting that certain linker-induced conformations are particularly favorable for RET. In contrast, the distribution for intermolecular pairs (Figure 3b) appears more diffuse, with a broad range of distances (up to 9 nm) and angles spread nearly uniformly between 0 and 180 deg. This random spatial arrangement stems from the less restricted nature of molecular packing in the film. However, specific intermolecular configurations still achieve high K^2 values, as indicated by the bright yellow regions in the plot, underscoring the potential for efficient RET even in a largely disordered system.

The electronic coupling values (V_{DA}) and their associated RET rates (k_{RET}) further clarify the differences between intra- and intermolecular interactions. As seen in Figure 3c, intramolecular RET rates peak at around 7×10^6 s^{-1}, with V_{DA} values reaching up to ∼0.003 eV. These rates follow a theoretical dipole−dipole distance dependence, emphasizing the geometric regularity imposed by the molecular architecture. On the other hand, Figure 3d shows that intermolecular RET rates can exceed 1.8×10^8 s^{-1}, nearly 25 times higher than their intramolecular counterparts. This enhancement arises despite the generally larger intermolecular distances due to occasional configurations yielding significantly stronger couplings (V_{DA} up to ∼ 0.020 eV). The 16 NEMD trajectories exhibit a consistent trend, with intermolecular energy transfer dominating over intramolecular transfer in the pure dyad film. Another representative trajectory from the NEMD simulations is illustrated in Figures S1 and S2.

Together, these observations suggest that although intramolecular RET benefits from well-defined geometries, intermolecular RET dominates the excited-state dynamics due to its much higher transfer rates and highly favorable D−A

https://doi.org/10.1021/acsaem.5c01620
ACS Appl. Energy Mater. XXXX, XXX, XXX−XXX

configurations within the disordered ensemble. This finding highlights the critical role of dynamic, nonbonded interactions in mediating long-range energy migration across the film. In MR-TADF-based donor−acceptor systems, such as the one studied here, tuning molecular packing to promote favorable intermolecular couplings may offer a viable strategy to enhance energy transfer and device performance.

To further understand how the theoretical RET rates manifest in the dynamics of energy migration, we performed kinetic Monte Carlo simulations for the pure dyad film (Figures 4 and S3). The decay profiles reveal distinct behaviors for intra- and intermolecular energy transfer pathways. The intramolecular energy transfer component exhibits a slower decay, with most peaks occurring below 25 μs, compared to the intermolecular counterpart, where peaks are predominantly observed below 10 μs. This observation is consistent with our earlier analysis, where intermolecular RET rates were found to be significantly higher—on the order of 10^8 s^{-1}—due to occasional shorter separation distances and stronger electronic couplings. The decay time distributions further highlight the kinetic disparity between the two mechanisms. Intermolecular energy transfer events (blue bars) are sharply concentrated within the 0−10 μs window, with nearly all decays occurring before 15 μs. The calculated average lifetimes of the intermolecular and intramolecular components are 3.2 and 12.8 μs, respectively. The high normalized frequency peaking near unity at the shortest decay times indicates that intermolecular RET is both rapid and consistent when favorable molecular configurations are present. This behavior aligns with the high K^2 values and strong V_{DA} (∼0.02 eV) previously observed for specific intermolecular geometries. In contrast, the intramolecular decay profile (green bars) is substantially broader, with decay events extending beyond 50 μs. Although the maximum frequency still occurs at short time scales, the pronounced tail in the distribution points to considerable variability in intramolecular RET dynamics. This variability arises from the range of conformational possibilities imposed by the cyclohexane linker, which introduces geometric constraints but also allows for occasional favorable alignments between donor and acceptor units. However, the generally weaker couplings (up to ∼0.003 eV) lead to slower and more dispersed energy transfer events.

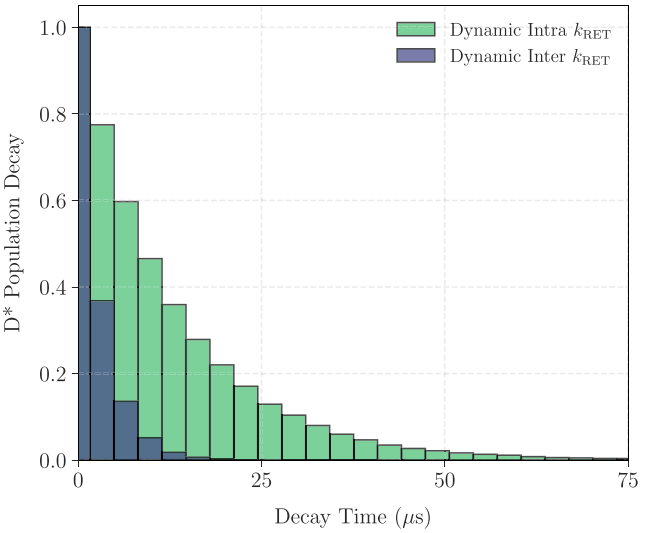

Figure 4. Kinetic Monte Carlo (kMC) simulated decay profile of the excited donor state (D*) in the pure dyad film, comparing intramolecular (green) and intermolecular (blue) energy transfer pathways. The plot illustrates the faster decay associated with intermolecular transfer due to higher electronic couplings and shorter donor−acceptor separations.

Overall, these simulations underscore how the interplay of geometry, coupling strength, and orientation factor governs the RET efficiency in pure film. The dominance of fast intermolecular decay suggests that energy migration across the film is primarily mediated through intermolecular hopping, enabling rapid and long-range energy transfer. Meanwhile, the slower intramolecular transfer acts as a supplementary pathway, contributing to intramolecular energy redistribution. These findings highlight the importance of molecular packing and local environments in modulating excited-state dynamics in MR-TADF dyad systems.

Having established the energy transfer characteristics in the pure dyad film, we now turn our attention to the doped system. Introducing a host environment leads to notable changes in morphology, as evident in Figure 5a. Unlike the relatively uniform distribution in the pure film, the doped system exhibits a multimodal distribution in the orientational order parameter (S), ranging from −0.4 to 1. This range reflects a broad spectrum of molecular orientations—from nearly horizontal to perfectly vertical—although the film remains globally isotropic. These diverse orientational states suggest that the host matrix imposes additional structural constraints on the dyad molecules.

As evident from Figure 5a, the intermolecular S distribution (blue) exhibits three distinct peaks at −0.35, 0.25, and 0.85, indicating a strong preference for horizontal orientation at −0.35, alongside two metastable configurations at 0.25 and 0.85. In contrast, the intramolecular S distribution (green) is less sharply defined but also displays three preferred orientations: a

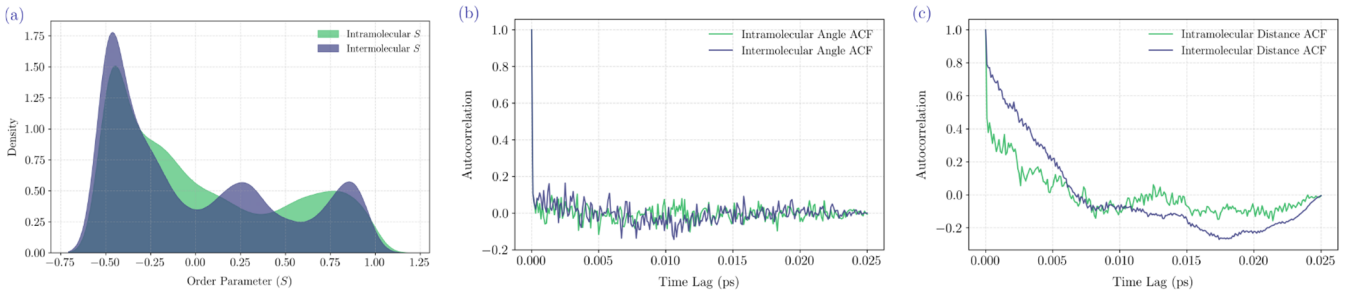

Figure 5. (a) Distribution of the order parameter S for the doped film, indicating overall isotropic molecular orientation with subtle intra- and intermolecular alignment preferences. (b) Angular autocorrelation functions show rapid decay of orientational correlations, reflecting dynamic molecular reorientation. (c) Distance autocorrelation functions highlight distinct temporal behaviors in intra- and intermolecular distances.

https://doi.org/10.1021/acsaem.5c01620
ACS Appl. Energy Mater. XXXX, XXX, XXX−XXX

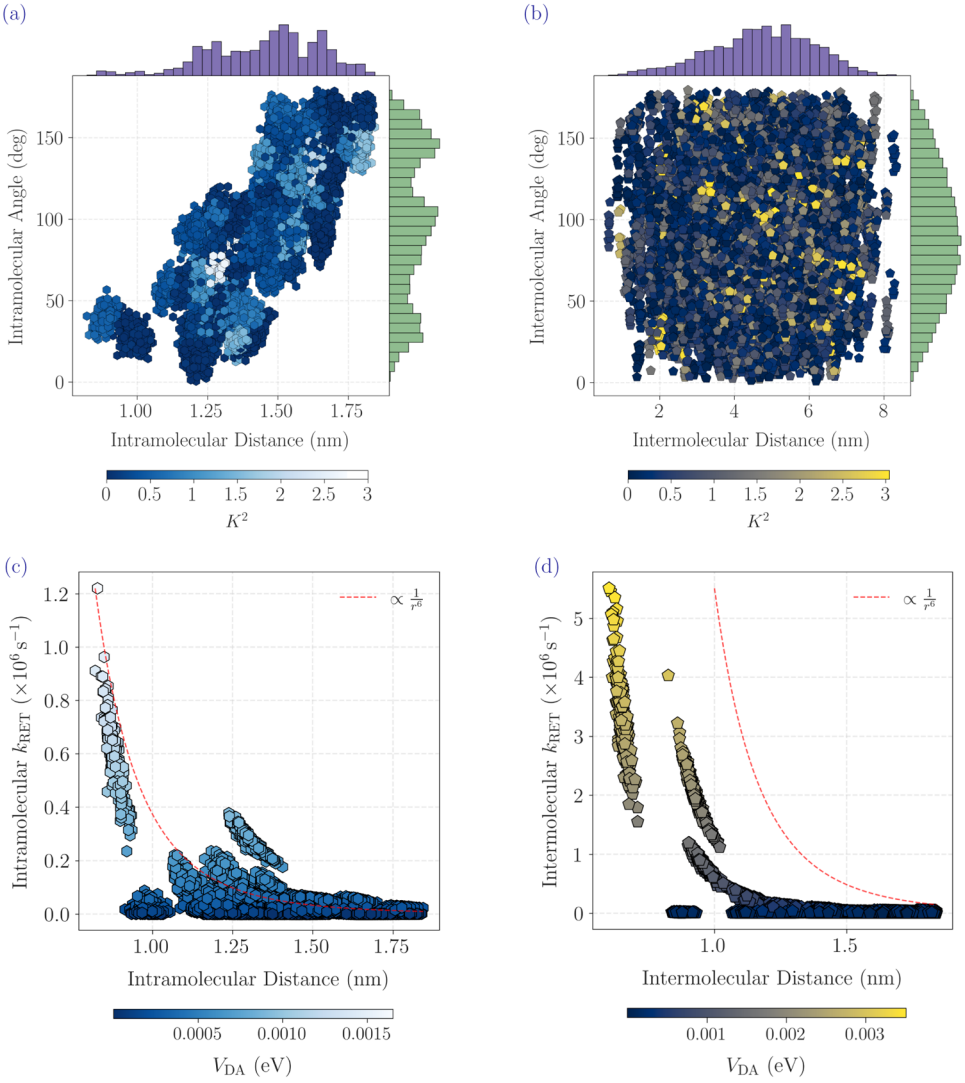

Figure 6. (a) Joint distribution of distance, angle, and orientation factor (K^2) for intramolecular donor−acceptor (D-A) pairs in the doped dyad film. (b) Corresponding distribution for intermolecular D−A pairs, showing more random geometries but occasional high K^2 values. RET rates (k_{RET}) versus electronic coupling (V_{DA}) for (c) intramolecular and (d) intramolecular interactions illustrate a distance-dependent trend. In panels (c) and (d), the dashed red line corresponds to a $\frac{1}{r^6}$ fit, consistent with the expected distance dependence.

prominent peak at −0.35, indicating strong horizontal alignment, and additional peaks at −0.15 and 0.85, corresponding to metastable states. The doped system clearly introduces a more structured and heterogeneous orientational landscape compared to the pure film, where orientation preferences were more subdued. Despite these pronounced static preferences, the angular autocorrelation functions (Figure 5b) for both intra- and intermolecular components decay rapidly—within 0.005 ps—indicating highly dynamic orientational fluctuations. Postdecay oscillations around zero reflect random reorientations with no long-term angular memory. The similar behavior of intra- and intermolecular angular correlations implies that the host matrix does not significantly differentiate between local and extended orientational dynamics.

The intermolecular distance ACF (blue) in the doped system decays more slowly than in the pure film (Figure 5c), suggesting enhanced spatial persistence in molecule−molecule separations, likely due to stabilizing interactions with host molecules. On the other hand, the intramolecular distance ACF (green) shows a more oscillatory pattern, indicative of complex periodic motions driven by the internal flexibility of the dyad and its interaction with the structured host environment. These results collectively demonstrate that doping induces both structural and dynamic reorganization in the film. The presence of multiple discrete orientational states and altered distance fluctuation profiles suggests that the host matrix not only modifies local molecular conformations but also imposes a more intricate energetic and spatial landscape. This has direct implications for resonance energy transfer: while the orientational distribution becomes more heterogeneous, the similar decay profiles in angle and distance correlations for intra- and intermolecular components suggest comparable fluctuation dynamics.

We now examine how doping influences the key parameters governing resonance energy transfer—namely, molecular distances, orientations, electronic couplings, and corresponding transfer rates. Compared to the pure film, the doped system displays a significant reorganization in these structural and electronic features, as illustrated in Figure 6. Panels (a) and (b) present the distance and angle distributions for intra- and intermolecular dyad pairs, respectively. The intramolecular

https://doi.org/10.1021/acsaem.5c01620
ACS Appl. Energy Mater. XXXX, XXX, XXX−XXX

donor−acceptor distance spans from 0.8 to 1.8 nm (Figure 6a), while intermolecular distances range widely from 0.6 to 8.3 nm (Figure 6b). While these distance distributions are qualitatively similar to those in the pure film, subtle shifts are evident. Most notably, the intermolecular distances are skewed toward larger values, with a histogram peak near 5−6 nm. This increase reflects the spatial separation enforced by the host matrix, which inhibits the close packing of dyad molecules and thus disrupts intermolecular coupling. Figure 6a further reveals the joint distribution of intramolecular distances and angles, with color-coded orientation factors (K^2). Three distinct conformational clusters emerge: one centered around 0.9−1 nm and 30−40 degrees, another around 1.1−1.3 nm and ∼105 degrees, and a broader distribution spanning 1.4−1.7 nm with angles between 120 and 150 degrees. The histogram confirms a preference for distances near 1.4−1.5 nm and a trimodal angle distribution with peaks at 30, 105, and 150 degrees. These discrete clusters imply that the doped environment restricts conformational flexibility, favoring a set of metastable dyad geometries. While K^2 values occasionally reach up to 3 in some geometries, the majority lie in the moderate-to-low range, suggesting limited dipole alignment across most conformers. Figure 6b shows that intermolecular distances in the doped system extend up to 9 nm, with a broad peak centered around 5−6 nm. Unlike the intramolecular angular distribution, intermolecular angles are more uniformly distributed from 0 to 180 deg, reflecting the isotropic nature of dyad orientations in the host matrix. While occasional high K^2 values (yellow regions) appear across the distance-angle plane, they are not concentrated in specific zones, highlighting the lack of persistent favorable alignments for energy transfer between dyad molecules in this environment.

The implications of these structural features are directly reflected in the RET rates and electronic couplings. Figure 6c displays the intramolecular rates, which peak at $\sim 1.2 \times 10^6\ s^{-1}$ at the shortest distances (∼0.8−0.9 nm), with corresponding V_{DA} values up to 0.0015 eV. Compared to the pure film, where intramolecular rates reached $\sim 7 \times 10^6\ s^{-1}$, this reduction indicates that the host matrix subtly perturbs the conformational ensemble of individual dyads, leading to less efficient internal energy transfer. Figure 6d highlights a more dramatic effect on intermolecular RET. The maximum rates fall to $\sim 5.5 \times 10^6\ s^{-1}$, with V_{DA} values reaching only ∼0.003 eV. This represents a nearly 30-fold reduction in maximum rate compared to the pure film (which reached $\sim 1.8 \times 10^8\ s^{-1}$). The significant increase in intermolecular separation, combined with more randomized orientations, severely limits efficient energy transfer pathways between molecules, demonstrating that the host molecules strongly suppress intermolecular coupling.

Interestingly, while both intra- and intermolecular RET rates follow the expected inverse dependence on distance, the distributions exhibit multiple distinct clusters or "branches," indicative of different configurational families with unique transfer characteristics. In the doped film, the maximum intermolecular to intramolecular rate ratio narrows to ∼4.5:1, in stark contrast to the ∼25:1 ratio observed in the pure system. This convergence suggests that doping selectively suppresses intermolecular energy transfer more strongly than intramolecular processes. These shifts are expected to strongly influence energy transfer dynamics in the doped film, potentially reducing transport range and introducing directional constraints on energy migration. Such insights are critical for designing host−guest systems with tailored optoelectronic performance.

The kMC simulations for the doped film (Figure 7) reveal a decay trend similar to the pure dyad system but with noticeably

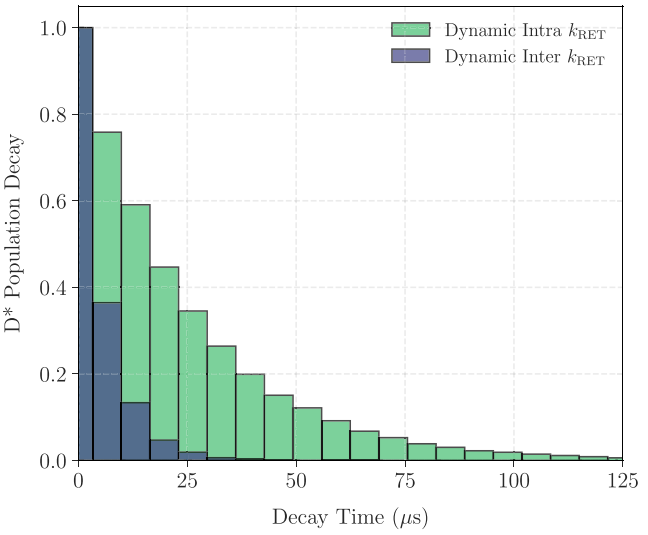

Figure 7. Kinetic Monte Carlo (kMC) simulated decay profile of the excited donor state (D*) in the doped dyad film, comparing intramolecular (green) and intermolecular (blue) energy transfer pathways.

slower dynamics for both intra- and intermolecular components. The average lifetimes of the intermolecular and intramolecular components for the doped system are 6.5 and 24.6 μs, respectively. These values are approximately twice those observed in the pure dyad system. This slowdown arises from the reduced dyad concentration and increased molecular spacing in the host matrix, which lowers energy transfer efficiency and extends the excited-state donor (D*) lifetime. Intermolecular transfer events (blue bars) exhibit sharp peaks within the first 15 μs—particularly between 0 and 5 μs—indicating rapid and efficient transfer occurring in rare, optimally aligned configurations. Compared to the pure film, these events are more temporally confined, reflecting fewer favorable intermolecular arrangements due to host-induced spatial separation. In contrast, intramolecular events (green bars) show a broader distribution, extending up to 125 μs, with peaks dominant below 50 μs. Although most occur early, a long tail suggests significant variation in intramolecular transfer times, likely due to conformational diversity among dyad molecules. Notably, intramolecular transfer plays a more prominent role in the doped system. The early time overlap of intra- and intermolecular events suggests both contribute initially, but the intramolecular pathway dominates over longer time scales. These results align with the previously observed reductions in RET rates and couplings, indicating that the host matrix selectively dampens energy transfer—particularly intermolecular—while reshaping the overall exciton migration landscape. This suggests a more complex, heterogeneous transport behavior in the doped film compared to the pure system.

Building upon the insights from the kMC analysis, which revealed distinct energy transfer behaviors in pure and doped films, we now turn to quantum chemical calculations to understand the nature of the excitons driving these processes. Specifically, we analyzed the interfragment charge transfer characteristics to probe the electronic coupling and exciton localization within the dyad (see Figure S4). Our analysis begins

https://doi.org/10.1021/acsaem.5c01620
ACS Appl. Energy Mater. XXXX, XXX, XXX−XXX

with the monomeric dyad (Table 1), where IFCT values confirm negligible charge transfer between all fragment pairs. This indicates the absence of significant through-bond charge transfer pathways. The complementary Independent Gradient Model based on Hirshfeld partitioning analysis (Figure S5) reveals minimal noncovalent interactions between the donor and the multiresonant core. Together, these results rule out the possibility of through-space charge transfer, confirming that the dyad's excited-state electronic structure is weakly coupled both through-bond and through-space.

Table 1. Inter-Fragment Charge Transfer (IFCT) Values for the Monomeric Dyad[a]

transferred electrons between fragments					
1 →3	0.00000	1 ←3	0.00011	Net 1 →3	−0.00011
2 →3	0.00000	2 ←3	0.00009	Net 2 →3	−0.00009
Intrinsic charge transfer percentage, CT(%): 0.020%					
Intrinsic local excitation percentage, LE(%): 99.980%					

[a]Fragment 1 corresponds to the cyclohexane bridge, fragment 2 to the donor unit, and fragment 3 to the multi-resonant (MR) core. Representative structure of the fragments is provided in Figure S4a of the SI. The low electron transfer values between fragments indicate negligible through-bond or through-space charge transfer, confirming the localized nature of excitation in the monomer. The IFCT values for only the non-zero charge-transfer are shown in the table. All other combinations of charge transfer are zero.

Table 2. Inter-Fragment Charge Transfer (IFCT) Analysis for the Dyad Dimer in the Pure Film[a]

transferred electrons between fragments					
1 →3	0.00001	1 ←3	0.00006	Net 1 →3	−0.00005
2 →3	0.00044	2 ←3	0.00014	Net 2 →3	−0.00030
2 →5	0.00000	2 ←5	0.00001	Net 2 →5	−0.00001
3 →5	0.00302	3 ←5	0.04344	Net 3 →5	−0.04042
3 →6	0.00000	3 ←6	0.00012	Net 3 →6	−0.00012
Intrinsic charge transfer percentage, CT(%): 4.724%					
Intrinsic local excitation percentage, LE(%): 95.276%					

[a]Fragment indices are defined as follows: 1 − cyclohexane bridge of monomer-I, 2 − donor fragment of monomer-I, 3 − acceptor (MR core) fragment of monomer-I, 4 − bridge fragment of monomer-II, 5 − donor fragment of monomer-II, and 6 − acceptor (MR core) fragment of monomer-II. The fragment structures are shown in Figure S4b of the SI. The table shows only the IFCT values corresponding to non-zero charge transfer; all other combinations exhibit zero charge transfer.

To explore exciton behavior in the solid state, we extended our analysis to a dyad dimer representative of the molecular arrangements in the pure film. The density difference plot (Figure 8a) suggests intermolecular charge transfer (CT), which is further substantiated by IFCT values (Table 2) and the transition density matrix (TDM) (Figure 8b). The TDM reveals a strong local excitation (LE) on the MR core (Fragment 5), a weak intermolecular CT between Fragments 3 and 5, and negligible intramolecular CT (between Fragments 2 and 3). These findings are consistent with the kMC results, where the pure film exhibited efficient energy transfer facilitated by close packing and stronger intermolecular couplings. Additionally, IGMH analysis (Figure 8c) identifies van der Waals interactions between donor−acceptor pairs, supporting the presence of favorable geometries that enhance intermolecular electronic communication.

In contrast, the doped system shows markedly different excitonic characteristics. The density difference plot (Figure 9a) and the TDM (Figure 9b) highlight a dominant LE character localized on Fragment 6, with minimal intermolecular CT and nearly absent intramolecular CT (confirmed by IFCT values, Table 3). The IGMH analysis (Figure 9c) reveals only weak donor−acceptor core interactions, suggesting an increased spatial separation between these fragments in the doped environment. This structural arrangement likely contributes to the reduced electronic coupling observed in both CT channels, further explaining the longer excited-state lifetimes and reduced RET rates found in the kMC analysis of the doped film.

Overall, the quantum chemical analysis reaffirms that in both systems, excitons are predominantly localized on the MR core. This is expected, given that the MR unit inherently includes both electron-donating and accepting sites, unlike traditional donor−acceptor systems. Consequently, local excitation dominates, with only limited CT contributions that are modulated by molecular packing. These results underscore how the doped host matrix structurally isolates dyad molecules, thereby

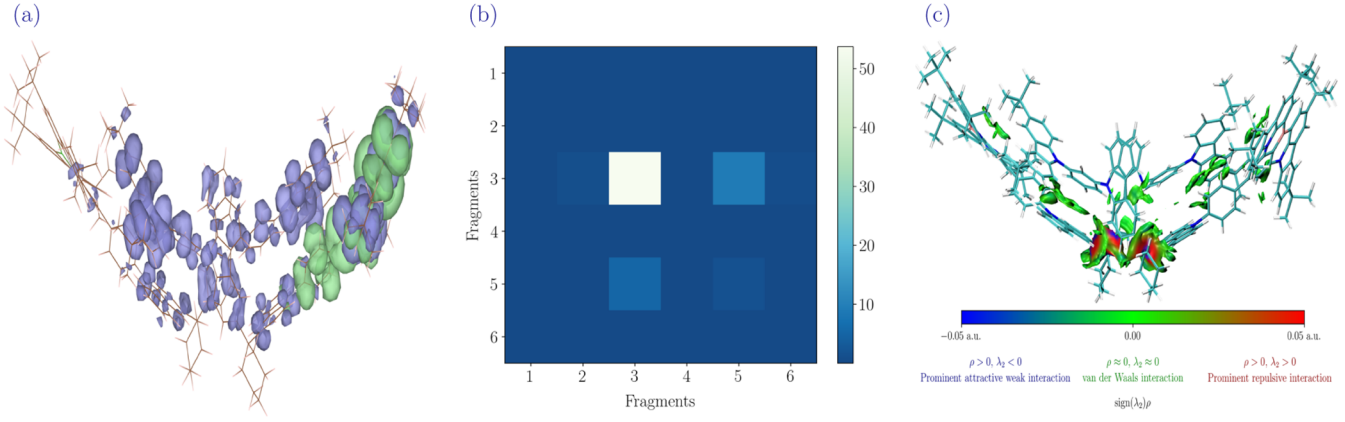

Figure 8. Electronic structure analysis of the pure dyad dimer. (a) Density difference plot illustrating the spatial distribution of electron density upon excitation, indicating possible intermolecular charge transfer. The violet regions represent areas of high electron density, while the green regions indicate electron-deficient zones. (b) Transition density matrix (TDM) highlighting the dominant local excitation (LE) on the MR core and weak intermolecular charge transfer (CT) pathways. (c) Independent Gradient Model based on Hirshfeld partition analysis, revealing van der Waals interactions between the dyad molecules, suggesting favorable packing that supports intermolecular coupling.

https://doi.org/10.1021/acsaem.5c01620
ACS Appl. Energy Mater. XXXX, XXX, XXX−XXX

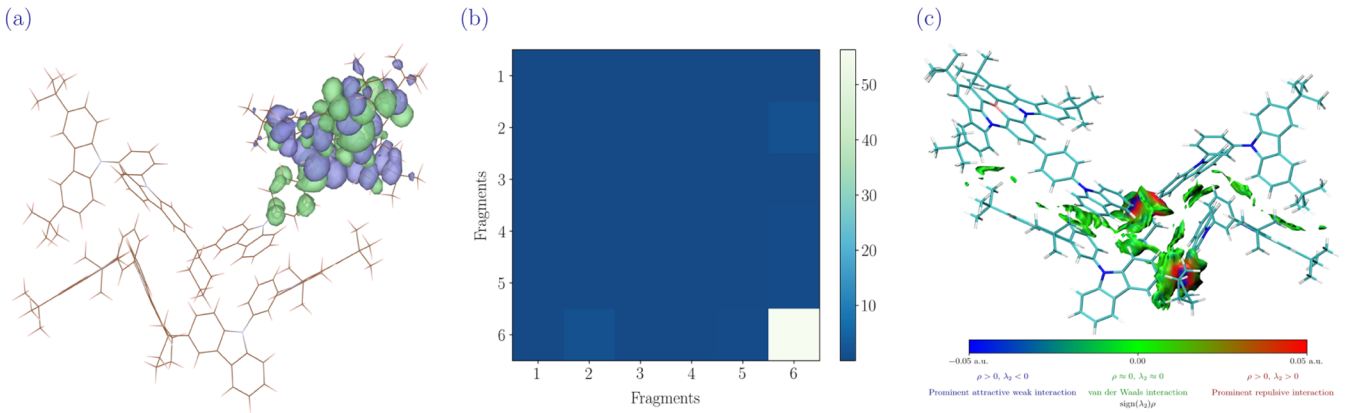

Figure 9. (a) Density difference plot for the donor host and the emitter dyad in the doped system. The violet color represents the electron-rich areas, and the green color indicates the electron-deficient regions. (b) The transition density matrix illustrates the nature and extent of various charge transfer pathways, highlighting dominant local excitation within the MR core. (c) IGMH analysis shows weak noncovalent interactions (green regions) between the donor host and the emitter dyad, indicating limited electronic coupling in the doped environment.

Table 3. Inter-Fragment Charge Transfer (IFCT) Analysis for the Doped Dimer System[a]

transferred electrons between fragments					
2 →6	0.00064	2 ←6	0.00030	Net 2 →6	0.00034
4 →6	0.00001	4 ←6	0.00005	Net 4 →6	−0.00004
5 →6	0.00005	5 ←6	0.00007	Net 5 →6	−0.00002
Intrinsic charge transfer percentage, CT(%): 0.112%					
Intrinsic local excitation percentage, LE(%): 99.888%					

[a]Fragment assignments are as follows: 1 − donor fragment of the host molecule, 2 − second donor fragment of the host, 3 − bridge fragment of the host, 4 − bridge fragment of the dyad, 5 − donor fragment of the dyad, and 6 − acceptor (MR core) fragment of the dyad. Representative structure of the fragments is provided in Figure S4c of the SI. The table includes only IFCT values with non-zero charge transfer, as all other combinations yield zero.

suppressing intermolecular interactions and altering the exciton dynamics compared to the pure film.

These findings underscore the potential of molecular and morphological engineering in optimizing energy transfer pathways for improved device performance. Increasing the doping concentration of the dyad molecule within the host matrix can significantly enhance intermolecular interactions, thereby promoting more efficient energy transfer and contributing to better device efficiency. However, while intermolecular transfer is tunable through concentration, a key limitation for intramolecular transfer lies in the large spatial separation between the donor and the MR core within the dyad. Addressing this bottleneck calls for targeted molecular design strategies—such as shortening the linker or implementing a rigid, macrocyclic-like architecture directly connecting the donor and acceptor fragments. These approaches could substantially reduce the intramolecular distance, enhance through-space electronic coupling, and ultimately unlock greater energy transfer efficiency.[40,41]

4. CONCLUSIONS

This work presents a comprehensive multiscale investigation into the morphology-dependent energy transfer behavior of emitter dyads in both pure and doped film architectures. By integrating molecular dynamics simulations with quantum mechanical calculations, we dissect the subtle trade-off between intra- and intermolecular energy transfer pathways that govern the photophysical performance of these systems. While the overall film morphologies appear isotropic, our analyses reveal a diverse distribution of molecular orientations—from horizontal to vertical—that critically modulate the orientation factor (K^2) and, consequently, the efficiency of resonance energy transfer.

In pure films, close molecular packing and favorable alignment between the donor and the multiresonant core facilitate efficient intermolecular RET. However, introducing a donor host in the doped film architecture dilutes the concentration of emitter dyads and disrupts their optimal spatial arrangement. This leads to increased intermolecular distances and a marked reduction in RET efficiency. Coarse-grained kinetic Monte Carlo simulations corroborate these observations: while pure films display rapid decay of excited donor populations—indicative of fast and efficient energy transfer—the doped films exhibit slower decay dynamics, reflecting the persistence of both intra- and intermolecular energy transfer events due to reduced dyad density and greater spatial separation.

To complement these morphological insights, we employed quantum chemical analyses using Inter-Fragment Charge Transfer and the Independent Gradient Model based on Hirshfeld partitioning. These calculations consistently highlight the predominance of locally excited (LE) states across both film types. Weak intermolecular charge transfer (CT) features emerge in the pure film, driven by favorable donor−acceptor proximity. In contrast, doped films significantly suppress CT contributions, attributable to the increased distance between the donor and MR fragments that limits through-space coupling.

In summary, our multiscale approach underscores the intricate interplay between molecular orientation, morphology, and energy transfer mechanisms in dyad-based emissive systems. These insights offer clear guidelines for rational design strategies—such as molecular engineering to enhance intramolecular interactions or morphological control to preserve favorable packing—that can ultimately optimize exciton dynamics and boost device performance in organic light-emitting applications.

■ ASSOCIATED CONTENT

Supporting Information

The Supporting Information is available free of charge at https://pubs.acs.org/doi/10.1021/acsaem.5c01620.

https://doi.org/10.1021/acsaem.5c01620
ACS Appl. Energy Mater. XXXX, XXX, XXX−XXX

Order parameters, autocorrelation functions, joint distribution plots, decay profile of the excited donor, IFCT, and IGMH analysis (PDF)

AUTHOR INFORMATION

Corresponding Author

Anirban Mondal − *Department of Chemistry, Indian Institute of Technology Gandhinagar, Gandhinagar, Gujarat 382355, India;* orcid.org/0000-0003-3029-8840; Email: amondal@iitgn.ac.in

Complete contact information is available at: https://pubs.acs.org/10.1021/acsaem.5c01620

Author Contributions

A.M. conceived the problem. N.R. conducted all the simulations. N.R. and A.M. analyzed the results and prepared the draft.

Notes

The data that support the findings of this study are available from the corresponding authors upon reasonable request.
The authors declare no competing financial interest.

ACKNOWLEDGMENTS

The authors gratefully acknowledge the Indian Institute of Technology Gandhinagar, India, for providing research facilities and financial support. We thank PARAM Ananta for computational resources.

REFERENCES

(1) Baldo, M. A.; Thompson, M. E.; Forrest, S. R. High-efficiency fluorescent organic light-emitting devices using a phosphorescent sensitizer. *Nature* **2000**, *403*, 750−753.

(2) Lu, L.; Guo, Y.; Zhao, B.; Wang, H.; Miao, Y. A new strategy to develop simple and efficient monochrome and white organic light-emitting diodes. *Mater. Today* **2024**, *74*, 109−120.

(3) Liu, H.; Liu, F.; Lu, P. Multiple strategies towards high-efficiency white organic light-emitting diodes by the vacuum deposition method. *J. Mater. Chem. C* **2020**, *8*, 5636−5661.

(4) Wang, G.; Kou, Z.; Jia, Z.; Guo, Z.; Xie, X.; Wanghe, R.; Ran, Z. Manipulating the energy transfer path to achieve a high-efficiency red fluorescent OLED by using a novel interface sensitization layer and multiple reverse intersystem crossing (RISC) channels. *J. Mater. Chem. C* **2025**, *13*, 7815−7823.

(5) Uoyama, H.; Goushi, K.; Shizu, K.; Nomura, H.; Adachi, C. Highly efficient organic light-emitting diodes from delayed fluorescence. *Nature* **2012**, *492*, 234−238.

(6) Heimel, P.; Mondal, A.; May, F.; Kowalsky, W.; Lennartz, C.; Andrienko, D.; Lovrincic, R. Unicolored phosphor-sensitized fluorescence for efficient and stable blue OLEDs. *Nat. Commun.* **2018**, *9*, No. 4990.

(7) Zhang, D.; Cai, M.; Bin, Z.; Zhang, Y.; Zhang, D.; Duan, L. Highly efficient blue thermally activated delayed fluorescent OLEDs with record-low driving voltages utilizing high triplet energy hosts with small singlet-triplet splittings. *Chem. Sci.* **2016**, *7*, 3355−3363.

(8) Furukawa, T.; Nakanotani, H.; Inoue, M.; Adachi, C. Dual enhancement of electroluminescence efficiency and operational stability by rapid upconversion of triplet excitons in OLEDs. *Sci. Rep.* **2015**, *5*, No. 8429.

(9) Nakanotani, H.; Higuchi, T.; Furukawa, T.; Masui, K.; Morimoto, K.; Numata, M.; Tanaka, H.; Sagara, Y.; Yasuda, T.; Adachi, C. High-efficiency organic light-emitting diodes with fluorescent emitters. *Nat. Commun.* **2014**, *5*, No. 4016.

(10) Haase, N.; Danos, A.; Pflumm, C.; Stachelek, P.; Brütting, W.; Monkman, A. P. Are the rates of dexter transfer in TADF hyperfluorescence systems optically accessible? *Mater. Horiz.* **2021**, *8*, 1805−1815.

(11) Xue, Q.; Xie, G. Thermally Activated Delayed Fluorescence beyond Through-Bond Charge Transfer for High-Performance OLEDs. *Adv. Opt. Mater.* **2021**, *9*, No. 2002204.

(12) Wang, X.-Q.; Yang, S.-Y.; Tian, Q.-S.; Zhong, C.; Qu, Y.-K.; Yu, Y.-J.; Jiang, Z.-Q.; Liao, L.-S. Multi-Layer π-Stacked Molecules as Efficient Thermally Activated Delayed Fluorescence Emitters. *Angew. Chem., Int. Ed.* **2021**, *60*, 5213−5219.

(13) Li, D.; Yang, J.; Chen, J.; Peng, X.; Li, W.; Chen, Z.; Qiu, W.; Yang, G.-X.; Yang, Z.; Li, M.; Jiang, S.; Liu, D.; Gan, Y.; Liu, K.; Su, S.-J. Efficient narrowband green OLEDs with TADF sensitizers combining multiple charge-transfer pathways. *Mater. Chem. Front.* **2023**, *7*, 1128−1136.

(14) Yang, Z.; Mao, Z.; Xu, C.; Chen, X.; Zhao, J.; Yang, Z.; Zhang, Y.; Wu, W.; Jiao, S.; Liu, Y.; Aldred, M. P.; Chi, Z. A sterically hindered asymmetric D-A-D' thermally activated delayed fluorescence emitter for highly efficient non-doped organic light-emitting diodes. *Chem. Sci.* **2019**, *10*, 8129−8134.

(15) Wang, J.; Miao, J.; Jiang, C.; Luo, S.; Yang, C.; Li, K. Engineering Intramolecular π-Stacking Interactions of Through-Space Charge-Transfer TADF Emitters for Highly Efficient OLEDs with Improved Color Purity. *Adv. Opt. Mater.* **2022**, *10*, No. 2201071.

(16) Anzola, M.; Sissa, C.; Painelli, A.; Hassanali, A. A.; Grisanti, L. Understanding Förster Energy Transfer through the Lens of Molecular Dynamics. *J. Chem. Theory Comput.* **2020**, *16*, 7281−7288.

(17) Wang, Z.; Cong, T. D.; Zhong, W.; Lau, J. W.; Kwek, G.; Chan-Park, M. B.; Xing, B. Cyanine-Dyad Molecular Probe for the Simultaneous Profiling of the Evolution of Multiple Radical Species During Bacterial Infections. *Angew. Chem., Int. Ed.* **2021**, *60*, 16900−16905.

(18) Leroy-Lhez, S.; Baffreau, J.; Perrin, L.; Levillain, E.; Allain, M.; Blesa, M.-J.; Hudhomme, P. Tetrathiafulvalene in a Perylene-3,4:9,10-bis(dicarboximide)-Based Dyad: A New Reversible Fluorescence-Redox Dependent Molecular System. *J. Org. Chem.* **2005**, *70*, 6313−6320.

(19) Jia, X.; Chen, Q.; Yang, Y.; Tang, Y.; Wang, R.; Xu, Y.; Zhu, W.; Qian, X. FRET-Based Mito-Specific Fluorescent Probe for Ratiometric Detection and Imaging of Endogenous Peroxynitrite: Dyad of Cy3 and Cy5. *J. Am. Chem. Soc.* **2016**, *138*, 10778−10781.

(20) Kwon, N. Y.; Kwak, H.; Kim, H. Y.; Park, S. H.; Park, J. Y.; Kang, M. J.; Koh, C. W.; Park, S.; Cho, M. J.; Choi, D. H. Effect of intramolecular energy transfer in a dual-functional molecular dyad on the performance of solution-processed TADF OLEDs. *Chem. Sci.* **2024**, *15*, 12361−12368.

(21) Lu, T. Sobtop: A Tool for Generating Force Field Parameters and GROMACS Topology Files 2025 http://sobereva.com/soft/Sobtop (accessed January 1).

(22) Lu, T. A Comprehensive Electron Wavefunction Analysis Toolbox for Chemists: Multiwfn. *J. Chem. Phys.* **2024**, *161*, No. 082503.

(23) Hess, B.; Kutzner, C.; van der Spoel, D.; Lindahl, E. GROMACS 4: Algorithms for Highly Efficient, Load-Balanced, and Scalable Molecular Simulation. *J. Chem. Theory Comput.* **2008**, *4*, 435−447.

(24) Pronk, S.; Páll, S.; Schulz, R.; Larsson, P.; Bjelkmar, P.; Apostolov, R.; Shirts, M. R.; Smith, J. C.; Kasson, P. M.; van der Spoel, D.; Hess, B.; Lindahl, E. GROMACS 4.5: a high-throughput and highly parallel open source molecular simulation toolkit. *Bioinformatics* **2013**, *29*, 845−854.

(25) Bussi, G.; Donadio, D.; Parrinello, M. Canonical sampling through velocity rescaling. *J. Chem. Phys.* **2007**, *126*, No. 014101.

(26) Berendsen, H. J. C.; Postma, J. P. M.; van Gunsteren, W. F.; DiNola, A.; Haak, J. R. Molecular dynamics with coupling to an external bath. *J. Chem. Phys.* **1984**, *81*, 3684−3690.

(27) Essmann, U.; Perera, L.; Berkowitz, M. L.; Darden, T.; Lee, H.; Pedersen, L. G. A smooth particle mesh Ewald method. *J. Chem. Phys.* **1995**, *103*, 8577−8593.

(28) Mondal, A.; Paterson, L.; Cho, J.; Lin, K.-H.; van der Zee, B.; Wetzelaer, G.-J. A. H.; Stankevych, A.; Vakhnin, A.; Kim, J.-J.; Kadashchuk, A.; Blom, P. W. M.; May, F.; Andrienko, D. Molecular Library of OLED Host Materials — Evaluating the Multiscale Simulation Workflow. *Chem. Phys. Rev.* **2021**, *2*, No. 031304.

(29) Frisch, M. J.; Trucks, G. W.; Schlegel, H. B.; Scuseria, G. E.; Robb, M. A.; Cheeseman, J. R.; Scalmani, G.; Barone, V.; Petersson, G. A.; Nakatsuji, H.; Li, X.; Caricato, M.; Marenich, A. V.; Bloino, J.; Janesko, B. G.; Gomperts, R.; Mennucci, B.; Hratchian, H. P.; Ortiz, J. V.; Izmaylov, A. F.; Sonnenberg, J. L.; Williams-Young, D.; Ding, F.; Lipparini, F.; Egidi, F.; Goings, J.; Peng, B.; Petrone, A.; Henderson, T.; Ranasinghe, D.; Zakrzewski, V. G.; Gao, J.; Rega, N.; Zheng, G.; Liang, W.; Hada, M.; Ehara, M.; Toyota, K.; Fukuda, R.; Hasegawa, J.; Ishida, M.; Nakajima, T.; Honda, Y.; Kitao, O.; Nakai, H.; Vreven, T.; Throssell, K.; Montgomery, J. A., Jr.; Peralta, J. E.; Ogliaro, F.; Bearpark, M. J.; Heyd, J. J.; Brothers, E. N.; Kudin, K. N.; Staroverov, V. N.; Keith, T. A.; Kobayashi, R.; Normand, J.; Raghavachari, K.; Rendell, A. P.; Burant, J. C.; Iyengar, S. S.; Tomasi, J.; Cossi, M.; Millam, J. M.; Klene, M.; Adamo, C.; Cammi, R.; Ochterski, J. W.; Martin, R. L.; Morokuma, K.; Farkas, O.; Foresman, J. B.; Fox, D. J. *Gaussian16 Revision C.01*; Gaussian Inc.: Wallingford CT., 2016.

(30) Lakowicz, J. R. *Principles of Fluorescence Spectroscopy*, 3rd ed.; Springer US: New York, NY, 2006.

(31) Fujimoto, K. J.; Miyashita, T.; Dewa, T.; Yanai, T. Determination of FRET orientation factor between artificial fluorophore and photosynthetic light-harvesting 2 complex (LH2). *Sci. Rep.* **2022**, *12*, No. 15091.

(32) Lee, C.-H.; Kim, S.-H.; Lee, H.; Seol, T. H.; Lee, J.-H.; Yi, Y.; Lee, G.-D. In Situ Substrate Temperature Control for High-Performance Blue-Emitting OLEDs with Extended Operational Lifetime. *ACS Appl. Mater. Interfaces* **2025**, *17*, 15755−15763.

(33) Afzal, M. A. F.; Cheng, C.; Hachmann, J. Combining first-principles and data modeling for the accurate prediction of the refractive index of organic polymers. *J. Chem. Phys.* **2018**, *148*, No. 241712.

(34) Gowers, R.J.; Linke, M.; Barnoud, J.; Reddy, T. J. E.; Melo, M. N.; Seyler, S. L.; Domański, J.; Dotson, D. L.; Buchoux, S.; Kenney, I. M.; Oliver, B.*MDAnalysis: A Python Package for the Rapid Analysis of Molecular Dynamics Simulations*, Proceedings of the 15th Python in Science Conference, 2016; pp 98−105.

(35) Michaud-Agrawal, N.; Denning, E. J.; Woolf, T. B.; Beckstein, O. MDAnalysis: A toolkit for the analysis of molecular dynamics simulations. *J. Comput. Chem.* **2011**, *32*, 2319−2327.

(36) Bannwarth, C.; Caldeweyher, E.; Ehlert, S.; Hansen, A.; Pracht, P.; Seibert, J.; Spicher, S.; Grimme, S. Extended tight-binding quantum chemistry methods. *WIREs Comput. Mol. Sci.* **2021**, *11*, No. e1493.

(37) Neese, F. The ORCA program system. *WIREs Comput. Mol. Sci.* **2012**, *2*, 73−78.

(38) Xu, J.; Dai, Y.; Zhang, J.; Jia, Z.; Meng, Q.; Qiao, J. Concerted Intramolecular and Intermolecular Charge Transfer for High-Efficiency Near-Infrared Thermally Activated Delayed Fluorescent Materials Approaching 900 nm. *Adv. Opt. Mater.* **2024**, *12*, No. 2300989.

(39) Lu, T.; Chen, Q. Independent gradient model based on Hirshfeld partition: A new method for visual study of interactions in chemical systems. *J. Comput. Chem.* **2022**, *43*, 539−555.

(40) Dnyaneshwar Veer, S.; Chandrakant Wakchaure, V.; Asokan, K.; Dixit, R.; Goswami, T.; Saha, R.; Gonnade, R.; Ghosh, H. N.; Santhosh Babu, S. Oligothiophene-Ring-Strapped Perylene Bisimides: Functionalizable Coaxial Donor−Acceptor Macrocycles. *Angew. Chem., Int. Ed.* **2023**, *62*, No. e202212934.

(41) Bold, K.; Stolte, M.; Shoyama, K.; Krause, A.-M.; Schmiedel, A.; Holzapfel, M.; Lambert, C.; Würthner, F. Macrocyclic Donor-Acceptor Dyads Composed of Oligothiophene Half-Cycles and Perylene Bisimides. *Chem. - Eur. J.* **2022**, *28*, No. e202200355.

https://doi.org/10.1021/acsaem.5c01620
ACS Appl. Energy Mater. XXXX, XXX, XXX−XXX